

The Topography Trap: Sifting Interlayer Excitons from Strain-Related Artifacts in Real-World 2D Heterostructures

Pablo Hernández López,¹ Luka Pirker,² Astrid Weston,³ Arijit Kayal,² Rafael Nadas,¹ Adrián Dewambrechies Fernández,⁴ Álvaro Rodríguez,⁵ Roman Gorbachev,³ Kirill I. Bolotin,⁴ Otakar Frank,^{2,*} and Sebastian Heeg^{1,†}

¹*Institut für Physik and Center for the Science of Materials Berlin, Berlin, Germany*

²*J. Heyrovsky Institute of Physical Chemistry,
Czech Academy of Sciences, Prague, Czech Republic*

³*Department of Physics and Astronomy and National Graphene Institute,
University of Manchester, Manchester, UK*

⁴*Physics Department, Freie Universität Berlin, Berlin, Germany*

⁵*Departamento de Física de la Materia Condensada
and Condensed Matter Physics Center (IFIMAC),
Universidad Autónoma de Madrid, Madrid, Spain*

(Dated: May 21, 2026)

KEYWORDS

Interlayer excitons; TMDC heterostructures; Tip-enhanced photoluminescence; Infrared photoluminescence; Momentum-indirect excitons; Bubbles

ABSTRACT

Novel excitonic phenomena emerging in transition metal dichalcogenide (TMDC) heterostructures belong to the most exciting topics in contemporary physics of van der Waals materials. Interlayer excitons (IXs) stand out among those due to their long radiative lifetimes and tunability by electric fields, strain, and twist angle. However, many ambiguities persist in the optical identification and manipulation of IXs, highlighting the need for reliable spectroscopic criteria that distinguish interlayer species from spurious signals. Here, we present a decision-tree protocol that evaluates interlayer coupling via intralayer exciton quenching and correlates photoluminescence (PL) with atomic force microscopy (AFM) to correctly assign room-temperature PL features in TMDC-based heterostructures. Applying this protocol, we identify momentum-direct IX between the K valleys of the two layers (KK-IX) in MoS₂-MoSe₂ and MoS₂-WSe₂ heterostructures at room temperature. In contrast, our protocol contests the reported bright, momentum-indirect, twist-angle-independent Γ K-IX in MoS₂-WSe₂. Comprehensive experimental data, including infrared and tip-enhanced photoluminescence (TEPL) with sub-diffraction-limited resolution, show no compelling evidence for this excitonic species, despite numerous reports. Instead, the spectroscopic features previously assigned to this Γ K-IX originate from locally strained WSe₂ at topographical inhomogeneities of the heterostructure interface, underscoring the need for robust, spatially resolved characterization of real-world samples in this highly accessible field and providing a generally applicable framework for identifying interlayer excitons in 2D semiconductor heterostructures.

INTRODUCTION

Interlayer excitons (IXs) are bosonic quasiparticles composed of electrons and holes spatially separated in different layers of two-dimensional semiconductor heterostructures. This spatial separation gives rise to a permanent out-of-plane electric dipole moment [1, 2] and extended lifetimes [3, 4] relative to their intralayer counterparts. IXs are highly tunable, for example, by selecting the material combination [5], strain and twist-angle engineering [6, 7], or applying external electric and magnetic fields [8, 9]. Moreover, IXs can be generated, manipulated, and detected optically. These traits have attracted much attention to IXs as a platform for exploring complex correlated many-body states [8, 10–12] and for encoding and transmitting information [13–15].

Optical signatures attributed to IXs have been reported for all combinations of the four main TMDCs, see Table I, as well as for combinations of these TMDCs and other materials, see Supplementary Note 2. Interlayer excitons emit PL from the infrared to the visible spectral range, and their large binding energies make them stable up to room temperature [16]. Depending on whether the electron and hole reside in equivalent or different valleys in their corresponding band structure, IXs can be momentum-direct (e.g., KK) or indirect (e.g., Γ K or QK), respectively. Momentum-direct IXs are observed only in heterostructures with small twist angles θ , where the K valleys of two layers closely align [17]. In contrast, momentum-indirect IXs exhibit much weaker twist-angle dependence than their direct counterparts and can be detected at all orientations, relaxing fabrication constraints [16].

The combination of room temperature, visible-range PL emission, and weak twist-angle dependence (in momentum-indirect IX) makes IXs a highly accessible field across physics, chemistry, and material science. However, these experimental advantages, together with fabrication-related inhomogeneities such as strain and chemical residues in real-world samples [18–20], also increase the risks of mischaracterizing emissions resembling IXs. Conflicting reports exist on the direct or indirect nature of IXs in MoSe_2 – WSe_2 [21, 22] and WS_2 – WSe_2 heterostructures [23, 24], on the hybrid character of WS_2 – MoSe_2 excitons [25, 26] and on the existence of Γ K interlayer excitons in MoS_2 – WSe_2 [27, 28]. This calls for an experimental framework that guides the reliable characterization of IXs in TMDC-based heterostructures. Such guidance must build on widely available, room-temperature methods and instrumentation, as research in new excitonic species between TMDCs and other materials moves

Screening protocol for interlayer exciton photoluminescence on TMDC-based heterostructures

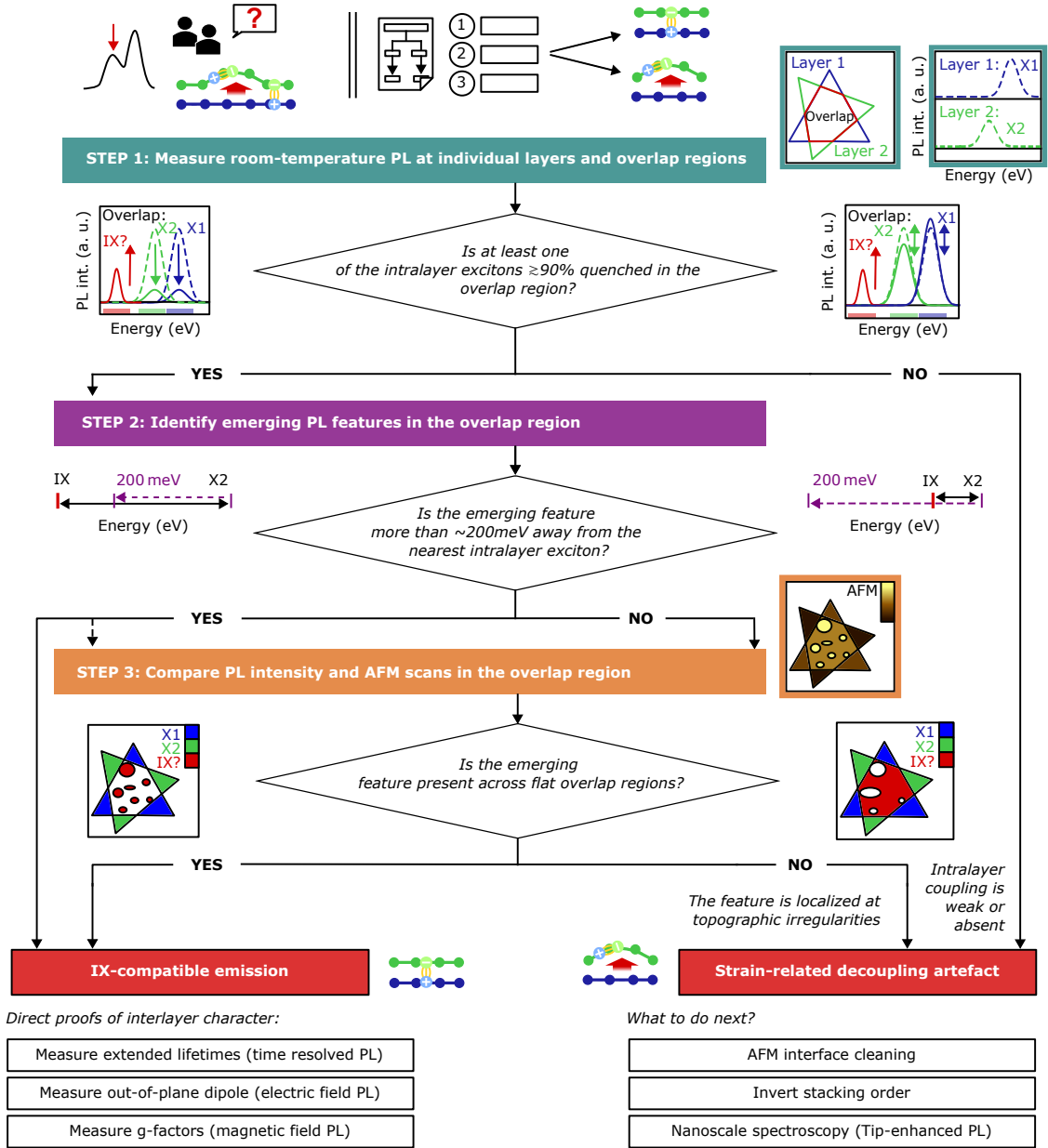


FIG. 1. **Screening protocol for interlayer exciton photoluminescence on TMDC-based heterostructures.** Decision tree with the key experimental steps to correctly identify emergent IX PL peaks in TMDC heterostructures and filter topography-related artifacts. We start collecting single PL spectra at the relevant areas in the sample. Intralayer exciton quenching relative to the isolated monolayers serves as a measure of interlayer coupling. For material combinations where IX lies within an approximate energy range of 200 meV from an intralayer exciton (see Table I), correlating PL intensity maps and AFM topography allows to determine whether the origin of the emergent PL peaks is compatible with IX emission or a strained intralayer exciton.

forward across multiple disciplines.

Combination TMDC1–TMDC2	Intralayer exciton X1 (eV)	Intralayer exciton X2 (eV)	IX (eV)	Energy separation X2-IX (meV)	IX Transition	Refs.
MoS ₂ –MoSe ₂	1.84	1.56	1.3-1.47	90-260	KK	[17, 29, 30]
MoS ₂ –WSe ₂	1.86	1.64	0.9, 1.02	650, 620	KK	[28, 31, 32]
	1.85	1.65	1.6	50	ΓK?	[27, 33]
WS ₂ –MoS ₂	1.98	1.87	1.45, 1.52, 1.63	420, 350, 240	ΓK, QK, KK	[34–36]
WS ₂ –MoSe ₂	1.98	1.49-1.57*	1.49-1.57*	-	*Hyb MoSe₂-IX	[25, 37]
WS ₂ –WSe ₂	1.95	1.63	1.39, 1.43	240, 200	ΓK/KK, KK/QK	[24, 38, 39]
WSe ₂ –MoSe ₂	1.66	1.57	1.33-1.38	190-240	KK/QK	[3, 7, 21, 22, 40]

TABLE I. **Reported energies of intra- and interlayer excitons at room temperature for all combinations of the four main TMDCs and assigned valley transition to the IX.** IX transition assignments with literature discrepancies are highlighted in bold. The energies for the MoSe₂ intralayer exciton and IX in WS₂–MoSe₂ are marked with an asterisk (*) as the observed corresponding excitonic species is reported to be a hybrid of intra- and interlayer exciton.

In this work, we introduce a protocol for screening suspected IX PL features at room temperature in TMDC-based heterobilayers (Figure 1). We first demonstrate the protocol by identifying the KK-IX in MoS₂–MoSe₂ and then use it to study the case of MoS₂–WSe₂, where both a KK-IX and a momentum-indirect ΓK-IX have been reported. Applying our protocol, we conclude that there is no evidence for ΓK-IX in MoS₂–WSe₂ heterostructures. Moreover, we perform TEPL spectroscopy with 20 nm spatial resolution to show that the PL features commonly attributed to ΓK-IX in MoS₂–WSe₂ actually originate from strained WSe₂ intralayer excitons emerging at topography irregularities in the heterostructure interface.

RESULTS AND DISCUSSION

Screening protocol for interlayer exciton photoluminescence

Figure 1 presents our proposed protocol to evaluate the compatibility of room-temperature PL features from TMDC heterostructures with IX emission. The aim of this decision-tree-based workflow is to be highly accessible. The protocol relies on standard experimental

techniques such as PL microspectroscopy and atomic force microscopy (AFM). Its applicability extends beyond combinations of the four main TMDCs and includes heterobilayers formed with non-conventional TMDCs (e.g., rhenium-based compounds and tellurides) as well as perovskites and molecules. We include an extended discussion of the applicability of the protocol in Supplementary Note 2. The main condition for a heterostructure to host IXs is a type-II band alignment between the constituent monolayers. A type-II or staggered band alignment drives charge transfer between the layers, spatially separating electrons and holes and thereby enabling the formation of IXs [16]. Prior knowledge of the band alignment, as well as the band-structure features of the constituent monolayers, allows us to estimate the expected emission energy range of IXs and thus provides an initial level of screening between genuine IX-like emission and strain-induced PL from individual monolayers.

We start the characterization of a heterobilayer in step 1 of Figure 1 by defining three significant areas on the sample: the two isolated monolayers and the overlap area forming the heterostructure. During fabrication, we intentionally avoid full overlap to use the PL of the isolated layers as a reference. In the overlap region, complete or almost complete quenching of intralayer excitons relative to their intensities in the individual layers indicates efficient charge transfer and therefore strong interlayer coupling. We discuss quantitative quenching factors for different material combinations in Supplementary Note 3. In contrast, the absence of quenching of intralayer excitons represents strong evidence of poor interlayer coupling, therefore questioning any further assignments to interlayer species.

After establishing that quenched intralayer emission confirms interlayer coupling, we proceed in Figure 1 with step 2 of the protocol, which requires looking for additional excitonic PL signatures in the energy range of the transition corresponding to the expected IX. Here, we want to make sure we distinguish real IXs from artifacts that may be emitting in the same energy range. Specifically, topographical irregularities in the overlap area can cause locally unquenched intralayer exciton emission that may be mistaken for interlayer species. These locally unquenched intralayer excitons are often downshifted in energy due to strain-driven band-gap reduction [41] and can overlap spectrally with IXs. We propose that the risk of strained intralayer excitons and IX overlapping is particularly high when the unstrained intralayer exciton and IX lie within 200 meV, requiring additional analysis. This threshold is

not fundamental but reflects typical tensile strains attainable at bubbles or wrinkles and the corresponding exciton shift rates reported for TMDC monolayers [28, 42, 43]. Combining the emission energies with information on intralayer exciton quenching, spatial characterization of emergent PL features, and sample topography is therefore crucial for a correct interpretation of the spectroscopic results.

Next, we perform hyperspectral PL mapping and AFM imaging and compare PL intensity maps and AFM topography, step 3 of Figure 1. Our goal is to examine the spatial origin of all PL emissions within 200 meV from the intralayer excitons. AFM topography reveals topographical features in the overlap area, including trapped contaminant pockets at the interface of the bilayer (or outside of it in the case of encapsulated samples), as well as cracks and folds, which range in size from tens to thousands of nanometers. We create PL maps of the emergent signal and the intralayer excitons, integrating PL intensity in the corresponding energy ranges. If PL intensity of the emergent signal is only present at the topography irregularities and absent in flat areas, we conclude that the emission in question is very unlikely to originate from interlayer species.

The spatial resolution of hyperspectral mapping should match the size of the topographical features in the sample to produce unequivocal maps. If topographical features are smaller than the light diffraction limit, spectroscopic techniques capable of reaching the corresponding lateral resolution, like TEPL, are necessary, as we demonstrate below. Further checks of the spectroscopic evidence of IXs, including contact-AFM interface cleaning and stacking order inversion, are described in Supplementary Note 4. For PL features that pass all three sifting steps in Figure 1, the protocol confirms their compatibility with IX emission and establishes a minimal standard for IX assignments based on room-temperature PL and AFM. This, however, does not constitute a direct, absolute proof of their interlayer character. We include a list of experiments that unambiguously confirm IX, namely the measurements of the extended lifetime [21], out-of-plane electric dipole [2], and characteristic g-factors [44].

KK-IX in MoS₂–MoSe₂ with $\theta \sim 0^\circ$

Having established the main analysis steps of our protocol in Figure 1, we apply it to a MoSe₂/MoS₂ heterobilayer with $\theta \sim 0^\circ$. In the following, we will separate the materials in a heterostructure with a dash (–) to indicate arbitrary stacking order and with a slash (/) to indicate that the first material is on top. In MoS₂–MoSe₂, an IX between the K valleys of MoS₂ and MoSe₂ is expected at 1.3 eV for twist angles close to 0° or 60° , where K valleys align, and the transition between them is momentum-direct [29]. We present in Figure 2a representative PL spectra from the relevant regions in the sample shown in Figure 2b, featuring the corresponding intralayer excitons at 1.9 eV (MoS₂, blue) and 1.6 eV (MoSe₂, orange) in the isolated monolayers, and a peak at 1.3 eV in the overlap region (red). Intralayer excitons in the overlap area are quenched by 86% (MoS₂) and 99% (MoSe₂) compared to the monolayer regions. This meets the condition in step 1 of the protocol. A KK-IX is expected at 1.3 eV, 300 meV away from the nearest intralayer emission, the MoSe₂ intralayer exciton. This satisfies the condition in step 2. Therefore, following the protocol in Figure 1, the feature is compatible with an IX at 1.3 eV. We include for completeness the spatial PL maps of the MoS₂ and MoSe₂ intralayer excitons, Figure 2c, and the KK-IX, Figure 2d. KK-IX is present in the overlap area but not in the isolated monolayers, while the intralayer excitons are most prominent in the corresponding isolated monolayers and in spatially restricted regions in the overlap area that coincide with sample irregularities (bubbles) seen in the AFM topography in Figure 2e.

KK-IX and no Γ K-IX in MoS₂–WSe₂ with $\theta \sim 0^\circ$

We now apply the protocol to re-examine the case of the MoS₂–WSe₂ heterostructure. We will focus on the two IXs reported in this system: the momentum-direct KK-IX and the momentum-indirect Γ K-IX. The intravalley KK-IX has been extensively reported in room temperature and cryogenic PL spectroscopy [31, 32, 45–49] at energies of ≈ 1 eV and directly imaged by ARPES [50, 51]. Its permanent out-of-plane dipole, direct proof of its interlayer character, has been measured through its Stark shift [31]. On the other hand, the momentum-indirect Γ K-IX PL in MoS₂–WSe₂ heterostructures was first reported in 2014

[33, 52]. Because the observed emission energy was above the interlayer bandgap [53–55], it was assigned to a momentum-indirect transition between the K and Γ points [27, 56]. Many works have followed, using room-temperature PL as the primary evidence for the existence of this novel IX, reported at various energies between 1.5 eV and 1.65 eV [57–62]. In the following, we will use our protocol to confirm the spectroscopic evidence for KK-IX and reject that for Γ K-IX in MoS₂–WSe₂ bilayers.

First, we characterize the KK-IX in a closely aligned 0° WSe₂/MoS₂ heterostructure. At $\theta \sim 0^\circ$ (60°), the corners of the Brillouin zones for the constituent layers align, giving rise to a momentum-direct, optically bright KK-IX. Additionally, the momentum-indirect Γ –K transition does not require any valley alignment and may therefore occur at all twist angles. Hence, in MoS₂–WSe₂ heterostructures with $\theta \sim 0^\circ$, both indirect and direct IX should be present.

Figure 2f shows representative infrared and visible room-temperature PL spectra of a WSe₂/MoS₂ sample from the points indicated in Figure 2g. The sample is fabricated via PC-mediated stacking of exfoliated monolayers and hBN-encapsulated to ensure cleanliness, see Methods in Supplementary Note 1 for details. At the individual monolayers, we observe MoS₂ (blue, 1.85 eV) and WSe₂ (green, 1.66 eV) intralayer excitons. In the overlap area, these intralayer excitons are quenched by >99% compared to the monolayers, and a new peak emerges at 1 eV, the energy of the KK transition, 600 meV away from the WSe₂ intralayer exciton. Following the protocol, we can safely assign this emerging peak to an IX. In the PL intensity map in Figure 2h, intralayer emission is present in the individual monolayers but is completely quenched in the heterostructure. In contrast, in Figure 2i, KK-IX emission is present only in the heterostructure region and absent in the isolated monolayers. These observations clearly confirm that the conditions for the formation of IX are fully met everywhere in the heterostructure area. However, we do not observe any PL emission in the spectral region between 1.4 eV and 1.6 eV, where the momentum-indirect Γ K-IX exciton has been reported [27]. The theoretical framework of the Γ K-IX does not support a scenario in which the exciton is absent for $\theta \sim 0^\circ, 60^\circ$ but present for all other angles. Our observations strongly suggest the absence of optically bright momentum-indirect, twist-angle independent IX in MoS₂–WSe₂ heterobilayers.

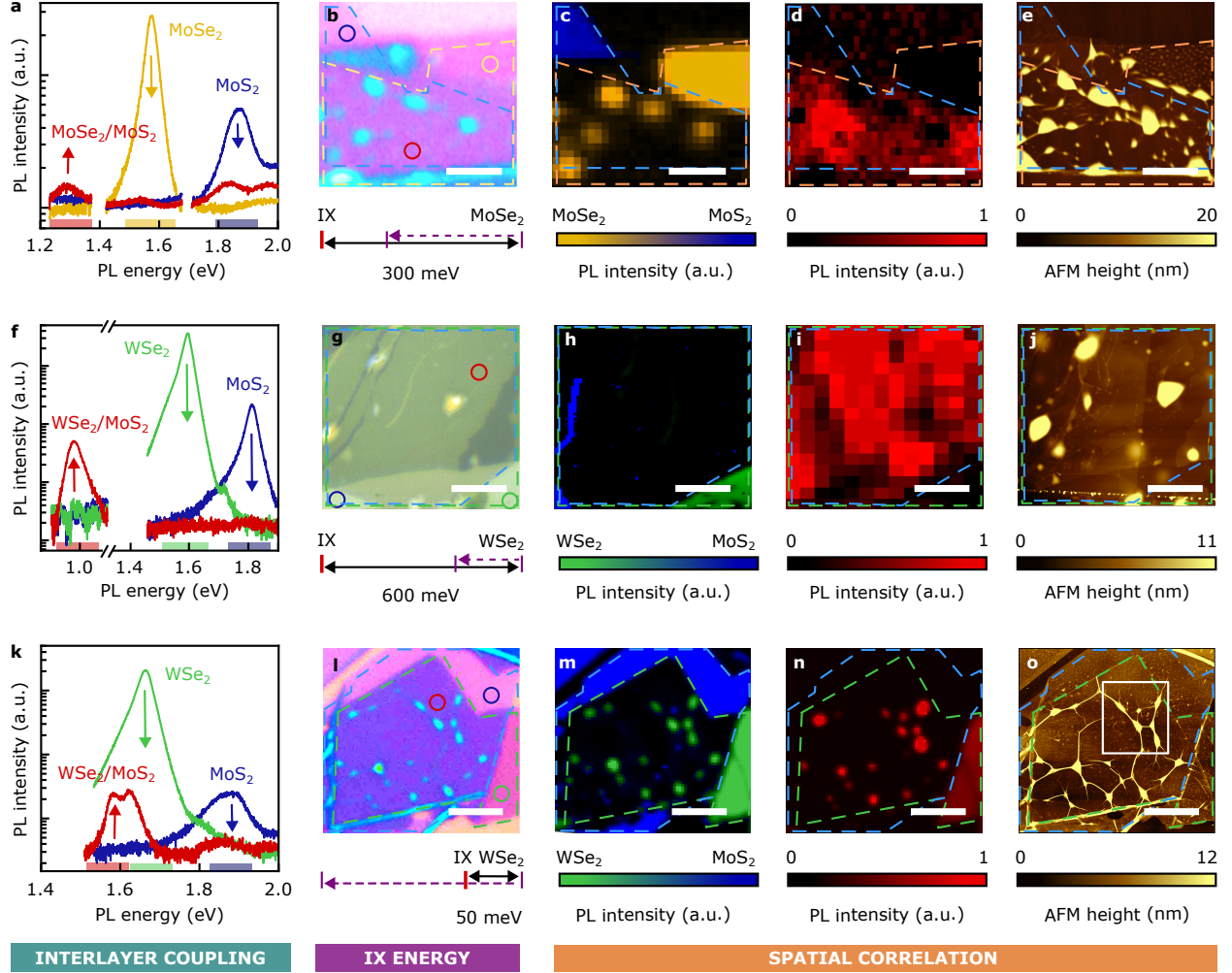


FIG. 2. Screening interlayer excitons in TMDC-based heterostructures. Sequential characterization, following the protocol in Figure 1, of KK-IX in MoS₂-MoSe₂ (a–e, passes the protocol), and KK-IX (f–j, pass) and Γ K-IX in MoS₂-WSe₂ (k–o, fail). (a, f, k) Representative infrared (a,f) and visible (a, f, k) PL spectra collected at the points marked with the same color in the microscope images of the heterostructures. PL intensity on a log scale. (b, g, l) Schematic of the energy distance between IX and the nearest intralayer exciton. Purple arrows mark the 200 meV threshold proposed in step 2 of the protocol. (c, h, m) PL intensity maps of the corresponding intralayer excitons. (d, i, n) PL intensity maps of KK-IX (d, i) and the 1.6 eV feature misattributed to a Γ K-IX (n). (e, j, o) AFM topography maps with cropped height range. Full-range maps in Supplementary Figure S6. The white square in (o) marks the area analyzed in Figure 3. Scale bars: b,c,d,e: 4 μ m, g,h,i,j: 10 μ m, l,m,n,o: 3 μ m.

Strain, not Γ K-IX in MoS₂-WSe₂ with $\theta > 0^\circ$

Next, we search for the true origin of the features that have been previously assigned to MoS₂-WSe₂ Γ K-IX by applying the protocol in Figure 1 to a WSe₂/MoS₂ heterostructure with $\theta > 0^\circ$. We fabricate a sample through PDMS-mediated dry transfer, as it is usually done in the literature, see Supplementary Note 1. In general, the use of PDMS introduces hydrocarbon-based contaminants at the interface, which coalesce during annealing into bubbles. These bubbles give rise to inhomogeneities in the sample topography that may cause misleading PL emission, a typical situation in real-world heterostructure devices fabricated by dry-transfer methods, which will be tested by our protocol.

Figure 2k shows representative PL spectra from the locations indicated in Figure 2l. Compared to the monolayer regions, the spectrum from the overlap area (red) features 99% (WSe₂) and 85% (MoS₂) quenched intralayer excitons PL and an additional PL peak at 1.59 eV, which may be interpreted as the indirect Γ K-IX. The emerging feature lies only 50 meV below the intralayer WSe₂ exciton. Following step 3 in the protocol, we compare hyperspectral maps (Figures 2m,n) and AFM topography (Figure 2o) to accurately determine the origin of the peak. WSe₂ and MoS₂ intralayer excitons dominate the individual layers and are almost fully quenched in a large part of the heterostructure region. However, the PL peak emerging around 1.59 eV (red spots in Figure 2n) appears only when the intralayer PL remains unquenched (green spots in Figure 2m) and is absent otherwise.

Indeed, there is a clear spatial correlation between the unquenched WSe₂ intralayer PL, Figure 2m, the PL feature at 1.59 eV, Figure 2n, and the bubbles in the AFM topography, Figure 2o. The same pattern is also apparent in the microscope image, Figure 2k. Bubbles locally decouple WSe₂ from the underlying MoS₂, reducing PL quenching, and induce strain, which redshifts the intralayer emission from the top layer. We now focus on the area of the sample marked with a white square in Figure 2o. Figure 3a shows exemplary PL spectra from the bubbles marked in Figure 3b. Spectra near bubbles may feature one shifted peak, as in curves 1, 2, or 3, or two distinct peaks, as in curves 4 and 5. This double peak feature

occurs when the laser spot probes areas with varying strain, such as two differently strained bubbles, collecting emission from both. For example, blue dashed lines in Figure 3a mark how curve 4 includes overlapping contributions from the neighboring bubbles measured in curves 1, 2, and 3. The observed downshifts of 20–80 meV correspond to 0.2–0.7% hydrostatic strain [63] and shift the WSe_2 intralayer exciton energy into the range at which the indirect IX has previously been reported. Note that a comparable analysis of the double peak is not available in the ΓK -IX literature, which largely neglects a thorough spatial characterization that compares PL maps and microscope images or AFM topography. [32, 45–49, 64].

TEPL of a $\text{WSe}_2/\text{MoS}_2$ heterostructure

Finally, we illustrate one of the additional spectroscopic checks proposed at the end of the protocol of Figure 1, performing TEPL with nanoscale spatial resolution on one of the contaminant bubbles visible in Figure 2l-o. TEPL shows unequivocally that bubble-induced strain in WSe_2 gives rise to the PL incorrectly attributed to ΓK -IX. We look at the ~ 200 nm bubble labeled 1 in Figure 3b. This bubble produces the lowest energy PL feature of the sample, see curve 1 in Figure 3a. We perform TEPL in the region marked with a white square in Figure 3c. The gain in lateral resolution is apparent comparing a 20 nm resolved TEPL linescan across the bubble with the corresponding confocal PL and AFM topography linescans, Figure 3d. The TEPL intensity map is shown in Figure 3e. Representative TEPL spectra along the line profile next to (A) and on (B) the bubble are shown in Figure 3f. Combined, they show that redshifted PL originates exclusively from the strained WSe_2 bubble. PL from the surrounding, well-coupled areas is completely quenched.

Local decoupling and straining of WSe_2 at topographical irregularities produce a big diversity of PL signals in energy and shape. The energy of PL from strained WSe_2 may depend indirectly on sample parameters like substrate adhesion, which influences the bubble strain [65], or twist angle, which modifies the interlayer coupling via atomic reconstruction [66]. The shape of PL from strained WSe_2 may vary with strain inhomogeneity (see, for example, Figure 3a), which depends on bubble size, shape, and distribution, as well as on strain-induced hybridization [67]. Crucially, as it is shown with the dashed vertical lines in

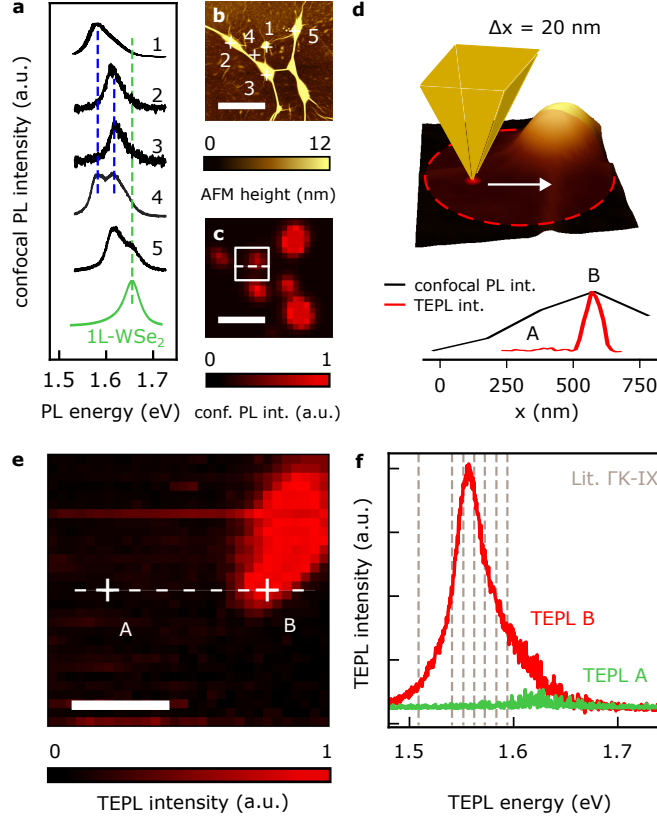


FIG. 3. Resolving the topography trap with TEPL. TEPL provides the nanoscale spatial resolution required when the protocol encounters sub-diffraction-limited topographical features, conclusively linking the emergent low-energy PL to strained WSe_2 rather than to an IX. (a) Representative confocal PL spectra collected at positions marked in (b) and unstrained WSe_2 for reference (green). Blue dashed lines: curve 4 consists of overlapping contributions from bubbles measured in curves 1, 2, and 3. (b) Detail of AFM topography of the sample in Figure 2j (c) Confocal PL intensity map between 1.45–1.65 eV for the same region. (d) Schematic of the TEPL measurement. The area shaded in red corresponds to the confocal laser spot. Inset: linecuts of confocal and TEPL intensity across a bubble corresponding to dashed lines in (c) and (e), respectively. (e) TEPL map at the white square in (c). (f) Representative TEPL spectra from (e). Grey dashed lines: Reported energies misassigned to a $\Gamma\text{K-IX}$. From left to right: Refs. [59, 33, 61, 57, 60, 27, 52]. Scale bars are $1.5 \mu\text{m}$ (b,c) and 100 nm (d).

Figure 3f, the energy range of these strain-induced PL features almost perfectly matches the energy range reported for the absent $\Gamma\text{K-IX}$ in the literature.

Discussion

Applying our IX PL screening protocol to the features hitherto identified as Γ K-IX in MoS₂–WSe₂ heterobilayers reveals a clear incompatibility with interlayer emission. A summary and extended discussion of our arguments against the existence of a bright Γ K-IX in MoS₂–WSe₂ is provided in Supplementary Note 5. Given the strong and robust evidence against bright, momentum-indirect, twist-angle independent IX in this system, our study calls for efforts to clarify the nature of experimental observations attributed to the Γ K-IX. This pertains to alleged properties such as tunability by mechanical strain [59], dominating radiative decay after ultrafast photo-excited charge transfer [68], robustness against charge-carrier doping [61], as well as the foundational demonstration of a room temperature excitonic transistor based on the electric control of Γ K-IX flux [57].

Beyond MoS₂–WSe₂, our work establishes a practical, room-temperature framework for assessing whether PL features in TMDC heterostructures are compatible with interlayer exciton emission. In its minimal form, a robust IX assignment should satisfy three criteria: (i) substantial quenching of intralayer excitons (typically $\gtrsim 90\%$ in at least one layer) demonstrating efficient interlayer charge transfer [21, 69], (ii) an IX energy that lies outside the strain-accessible redshift window of intralayer excitons (or, if within ~ 200 meV, is rigorously disentangled from strain-induced features), and (iii) an emergent PL signal that does not spatially correlate with topography-induced decoupling such as bubbles, wrinkles, or cracks. When these criteria are met, additional experiments that directly probe the interlayer character—such as lifetime measurements, Stark shifts, or characteristic g -factors—can elevate an IX-compatible assignment to a confirmed IX [1–3, 31, 44].

The detailed spatial characterizations suggested in our protocol, combining hyperspectral PL mapping, AFM topography, and, where necessary, TEPL with nanometer resolution, are also instrumental in advancing our understanding of confirmed IX within heterogeneous strain and dielectric landscapes. They provide direct insight into how local strain, interfacial cleanliness, and reconstruction reshape the excitonic potential landscape, which is particularly relevant in moiré superlattices and other engineered quantum materials [25, 47, 50, 64]. As device concepts increasingly rely on controlled exciton funnels, moiré trapping, and

long-range IX transport, such spatially resolved protocols become a prerequisite rather than an optional refinement.

By providing an accessible and standardized methodology based on widely available optical and topographic techniques, we aim to enhance the robustness and reproducibility of results derived from real-world heterostructures. The "topography trap" highlighted here is unlikely to be unique to MoS₂–WSe₂; it is a generic risk whenever interlayer species are inferred solely from PL at room temperature in samples with imperfect interfaces. Our decision-tree protocol therefore offers a generally applicable framework for reliably identifying interlayer excitons in 2D semiconductor heterostructures and for preventing artifacts from seeding entire research lines in this vibrant and rapidly expanding field.

CONCLUSIONS

We have introduced a room-temperature, decision-tree protocol that combines intralayer exciton quenching, energy placement within a realistic strain window, and spatial correlation of PL with AFM topography to sift genuine interlayer exciton emission from strain- and topography-induced artifacts in TMDC-based heterostructures. Applied to MoS₂–MoSe₂ and MoS₂–WSe₂ bilayers, the protocol robustly identifies momentum-direct KK-IX emission, but finds no compelling evidence for a bright, momentum-indirect, twist-angle-independent Γ K-IX in MoS₂–WSe₂. Instead, the corresponding PL features originate from locally decoupled and strained WSe₂ at interface bubbles and other topographical irregularities, exemplifying a generic “topography trap” in real-world 2D heterostructures.

Beyond this specific case, our work establishes a minimal standard for IX assignments based on room-temperature PL and AFM. This framework is readily applicable to other TMDC and moiré heterostructures, where local strain, reconstruction, and dielectric disorder reshape the excitonic landscape, and it complements direct probes of interlayer character. As the field moves toward scalable devices and complex excitonic architectures, adopting such protocol-driven standards will be essential to ensure that reported interlayer species are robust, reproducible, and suitable as reliable building blocks for future quantum and optoelectronic technologies.

ACKNOWLEDGMENTS

We acknowledge support by the German Research Foundation (DFG) and the Open Access Publication Fund of Humboldt-Universität zu Berlin. L.P. and O.F. acknowledge the support of the Ministry of Education, Youth, and Sports of the Czech Republic, Project No. CZ.02.01.01/00/22_008/0004558, co-funded by the European Union. L.P. and O.F. acknowledge the CzechNanoLab Research Infrastructure, supported by the Ministry of Education, Youth, and Sports of the Czech Republic (LM2023051). P.H.L., R.N., and S.H. acknowledge funding from the Deutsche Forschungsgemeinschaft (DFG, German Research Foundation) under the Emmy Noether Initiative (Project-ID 433878606). R.N. and S.H. acknowledge the DFG within the CRC 1772 mol2Dmat project (project numbers B02; project ID 555467911). KB acknowledges funding from BMFTR (05K2022 ioARPES) and DFG (CRC 1772, project B01, SPP2244).

DATA AVAILABILITY

All data supporting the key findings of this study shown in the article and the Supplementary Information file are available in Zenodo at <https://doi.org/10.5281/zenodo.20303868>. All raw data generated during the current study are available from the corresponding author upon request. Source data are provided with this paper.

* Correspondence email address: otakar.frank@jh-inst.cas.cz

† Correspondence email address: sebastian.heeg@physik.hu-berlin.de

- [1] Sigl, L. *et al.* Optical dipole orientation of interlayer excitons in MoSe₂-WSe₂ heterostacks. *Physical Review B* **105**, 035417 (2022).
- [2] Jauregui, L. A. *et al.* Electrical control of interlayer exciton dynamics in atomically thin heterostructures. *Science* **366**, 870–875 (2019).
- [3] Miller, B. *et al.* Long-lived direct and indirect interlayer excitons in Van der Waals heterostructures. *Nano Letters* **17**, 5229–5237 (2017).
- [4] Montblanch, A. R.-P. *et al.* Confinement of long-lived interlayer excitons in WS₂/WSe₂ heterostructures. *Communications Physics* **4** (2021).
- [5] Jiang, Y., Chen, S., Zheng, W., Zheng, B. & Pan, A. Interlayer exciton formation, relaxation, and transport in tmd Van der Waals heterostructures. *Light: Science & Applications* **10** (2021).
- [6] Zhang, D. *et al.* Enhancing layer-engineered interlayer exciton emission and valley polarization in Van der Waals heterostructures via strain. *ACS Nano* **18**, 17672–17680 (2024).
- [7] Nayak, P. K. *et al.* Probing evolution of twist-angle-dependent interlayer excitons in MoSe₂/WSe₂ Van der Waals heterostructures. *ACS Nano* **11**, 4041–4050 (2017).
- [8] Mak, K. F. & Shan, J. Opportunities and challenges of interlayer exciton control and manipulation. *Nature Nanotechnology* **13**, 974–976 (2018).
- [9] Holler, J. *et al.* Interlayer exciton valley polarization dynamics in large magnetic fields. *Physical Review B* **105**, 085303 (2022).
- [10] Wang, Z. *et al.* Evidence of high-temperature exciton condensation in two-dimensional atomic double layers. *Nature* **574**, 76–80 (2019).
- [11] Tang, Y. *et al.* Simulation of hubbard model physics in WSe₂/WS₂ moiré superlattices. *Nature* **579**, 353–358 (2020).
- [12] Xu, F. *et al.* Observation of integer and fractional quantum anomalous hall effects in twisted bilayer MoTe₂. *Physical Review X* **13**, 031037 (2023).
- [13] Ciarrocchi, A. *et al.* Polarization switching and electrical control of interlayer excitons in two-dimensional Van der Waals heterostructures. *Nature Photonics* **13**, 131–136 (2018).

- [14] Rivera, P. *et al.* Valley-polarized exciton dynamics in a 2D semiconductor heterostructure. *Science* **351**, 688–691 (2016).
- [15] Ye, T. *et al.* Nonvolatile electrical switching of optical and valleytronic properties of interlayer excitons. *Light: Science & Applications* **11** (2022).
- [16] Rivera, P. *et al.* Interlayer valley excitons in heterobilayers of transition metal dichalcogenides. *Nature Nanotechnology* **13**, 1004–1015 (2018).
- [17] Alexeev, E. M. *et al.* Nature of long-lived moiré interlayer excitons in electrically tunable MoS₂/MoSe₂ heterobilayers. *Nano Letters* **24**, 11232–11238 (2024).
- [18] Covre, F. S. *et al.* Revealing the impact of strain in the optical properties of bubbles in monolayer MoSe₂. *Nanoscale* **14**, 5758–5768 (2022).
- [19] Tilmann, R. *et al.* Identification of ubiquitously present polymeric adlayers on 2D transition metal dichalcogenides. *ACS Nano* **17**, 10617–10627 (2023).
- [20] Wang, W. *et al.* Clean assembly of Van der Waals heterostructures using silicon nitride membranes. *Nature Electronics* **6**, 981–990 (2023).
- [21] Rivera, P. *et al.* Observation of long-lived interlayer excitons in monolayer MoSe₂–WSe₂ heterostructures. *Nature Communications* **6** (2015).
- [22] Hanbicki, A. T. *et al.* Double indirect interlayer exciton in a MoSe₂/WSe₂ Van der Waals heterostructure. *ACS Nano* **12**, 4719–4726 (2018).
- [23] Jin, C. *et al.* Observation of moiré excitons in WSe₂/WS₂ heterostructure superlattices. *Nature* **567**, 76–80 (2019).
- [24] Wu, K. *et al.* Identification of twist-angle-dependent excitons in WS₂/WSe₂ heterobilayers. *National Science Review* **9** (2021).
- [25] Alexeev, E. M. *et al.* Resonantly hybridized excitons in moiré superlattices in Van der Waals heterostructures. *Nature* **567**, 81–86 (2019).
- [26] Guo, J. *et al.* Moiré-controllable exciton localization and dynamics through spatially-modulated inter- and intralayer excitons in a MoSe₂/WS₂ heterobilayer. *Nature Communications* **16** (2025).
- [27] Kunstmann, J. *et al.* Momentum-space indirect interlayer excitons in transition-metal dichalcogenide Van der Waals heterostructures. *Nature Physics* **14**, 801–805 (2018).
- [28] Rodriguez, A., Kalbáč, M. & Frank, O. Strong localization effects in the photoluminescence of transition metal dichalcogenide heterobilayers. *2D Materials* **8**, 025028 (2021).

- [29] Rodríguez, Á., Varillas, J., Haider, G., Kalbac, M. & Frank, O. Complex strain scapes in reconstructed transition-metal dichalcogenide moiré superlattices. *ACS nano* **17**, 7787–7796 (2023).
- [30] Mouri, S. *et al.* Thermal dissociation of inter-layer excitons in MoS₂/MoSe₂ hetero-bilayers. *Nanoscale* **9**, 6674–6679 (2017).
- [31] Karni, O. *et al.* Infrared interlayer exciton emission in MoS₂/WSe₂ heterostructures. *Physical Review Letters* **123**, 247402 (2019).
- [32] Tan, Q. *et al.* Layer-engineered interlayer excitons. *Science Advances* **7** (2021).
- [33] Fang, H. *et al.* Strong interlayer coupling in Van der Waals heterostructures built from single-layer chalcogenides. *Proceedings of the National Academy of Sciences* **111**, 6198–6202 (2014).
- [34] Gong, Y. *et al.* Vertical and in-plane heterostructures from WS₂/MoS₂ monolayers. *Nature Materials* **13**, 1135–1142 (2014).
- [35] Okada, M. *et al.* Direct and indirect interlayer excitons in a Van der Waals heterostructure of hBN/WS₂/MoS₂/hBN. *ACS Nano* **12**, 2498–2505 (2018).
- [36] Schottle, N. *et al.* Photophysics of direct and indirect interlayer excitons in MoS₂/WS₂ moiré superlattices. *ACS Photonics* **12**, 4670–4677 (2025).
- [37] Zhang, L. *et al.* Twist-angle dependence of moiré excitons in WS₂/MoSe₂ heterobilayers. *Nature Communications* **11** (2020).
- [38] Jin, C. *et al.* Identification of spin, valley and moiré quasi-angular momentum of interlayer excitons. *Nature Physics* **15**, 1140–1144 (2019).
- [39] Chen, J. *et al.* Twist-angle-dependent momentum-space direct and indirect interlayer excitons in WSe₂/WS₂ heterostructure. *RSC Advances* **13**, 18099–18107 (2023).
- [40] Tran, K. *et al.* Evidence for moiré excitons in Van der Waals heterostructures. *Nature* **567**, 71–75 (2019).
- [41] Niehues, I. *et al.* Strain control of exciton–phonon coupling in atomically thin semiconductors. *Nano Letters* **18**, 1751–1757 (2018).
- [42] Darlington, T. P. *et al.* Facile and quantitative estimation of strain in nanobubbles with arbitrary symmetry in 2D semiconductors verified using hyperspectral nano-optical imaging. *The Journal of Chemical Physics* **153** (2020).

- [43] Gastaldo, M. *et al.* Tunable strain and bandgap in subcritical-sized mos2 nanobubbles. *npj 2D Materials and Applications* **7** (2023).
- [44] Seyler, K. L. *et al.* Signatures of moiré-trapped valley excitons in MoSe₂/WSe₂ heterobilayers. *Nature* **567**, 66–70 (2019).
- [45] Liu, Y. *et al.* Room temperature nanocavity laser with interlayer excitons in 2D heterostructures. *Science Advances* **5** (2019).
- [46] Chen, D. *et al.* Spatial filtering of interlayer exciton ground state in WSe₂/MoS₂ heterobilayer. *Nano Letters* **24**, 8795–8800 (2024).
- [47] Tan, Q., Rasmita, A., Zhang, Z., Novoselov, K. & Gao, W.-b. Signature of cascade transitions between interlayer excitons in a moiré superlattice. *Physical Review Letters* **129**, 247401 (2022).
- [48] Tan, Q. *et al.* Layer-dependent correlated phases in WSe₂/MoS₂ moiré superlattice. *Nature Materials* **22**, 605–611 (2023).
- [49] Zhao, H. *et al.* Manipulating interlayer excitons for near-infrared quantum light generation. *Nano Letters* **23**, 11006–11012 (2023).
- [50] Karni, O. *et al.* Structure of the moiré exciton captured by imaging its electron and hole. *Nature* **603**, 247–252 (2022).
- [51] Schmitt, D. *et al.* Formation of moiré interlayer excitons in space and time. *Nature* **608**, 499–503 (2022).
- [52] Chiu, M.-H. *et al.* Spectroscopic signatures for interlayer coupling in MoS₂–WSe₂ Van der Waals stacking. *ACS Nano* **8**, 9649–9656 (2014).
- [53] Zhang, C. *et al.* Systematic study of electronic structure and band alignment of monolayer transition metal dichalcogenides in Van der Waals heterostructures. *2D Materials* **4**, 015026 (2016).
- [54] Zhang, C. *et al.* Interlayer couplings, moiré patterns, and 2D electronic superlattices in MoS₂/WSe₂ heterobilayers. *Science Advances* **3** (2017).
- [55] Ponomarev, E., Ubrig, N., Gutiérrez-Lezama, I., Berger, H. & Morpurgo, A. F. Semiconducting Van der Waals interfaces as artificial semiconductors. *Nano Letters* **18**, 5146–5152 (2018).
- [56] Latini, S., Winther, K. T., Olsen, T. & Thygesen, K. S. Interlayer excitons and band alignment in MoS₂/hBN/WSe₂ Van der Waals heterostructures. *Nano Letters* **17**, 938–945 (2017).
- [57] Unuchek, D. *et al.* Room-temperature electrical control of exciton flux in a Van der Waals heterostructure. *Nature* **560**, 340–344 (2018).

- [58] Nagler, P. *et al.* Interlayer excitons in transition-metal dichalcogenide heterobilayers. *physica status solidi (b)* **256** (2019).
- [59] Cho, C. *et al.* Highly strain-tunable interlayer excitons in MoS₂/WSe₂ heterobilayers. *Nano Letters* **21**, 3956–3964 (2021).
- [60] Ren, L. *et al.* Efficient modulation of MoS₂/WSe₂ interlayer excitons via uniaxial strain. *Applied Physics Letters* **120** (2022).
- [61] Khestanova, E. *et al.* Robustness of momentum-indirect interlayer excitons in MoS₂/WSe₂ heterostructure against charge carrier doping. *ACS Photonics* (2023).
- [62] Imaeda, K. *et al.* Plasmon-enhanced photoluminescence of interlayer excitons induced on WSe₂/MoS₂ heterobilayers. *The Journal of Physical Chemistry Letters* **17**, 1670–1676 (2026).
- [63] Kumar, A. M. *et al.* Strain fingerprinting of exciton valley character in 2D semiconductors. *Nature Communications* **15**, 7546 (2024).
- [64] Rosenberger, M. R. *et al.* Twist angle-dependent atomic reconstruction and moiré patterns in transition metal dichalcogenide heterostructures. *ACS Nano* **14**, 4550–4558 (2020).
- [65] Khestanova, E., Guinea, F., Fumagalli, L., Geim, A. K. & Grigorieva, I. V. Universal shape and pressure inside bubbles appearing in Van der Waals heterostructures. *Nature Communications* **7** (2016).
- [66] Weston, A. *et al.* Atomic reconstruction in twisted bilayers of transition metal dichalcogenides. *Nature Nanotechnology* **15**, 592–597 (2020).
- [67] Hernández López, P. *et al.* Strain control of hybridization between dark and localized excitons in a 2D semiconductor. *Nature Communications* **13** (2022).
- [68] Zimmermann, J. E. *et al.* Ultrafast charge-transfer dynamics in twisted MoS₂/WSe₂ heterostructures. *ACS Nano* **15**, 14725–14731 (2021).
- [69] You, W. *et al.* Strong interfacial coupling in vertical WSe₂/WS₂ heterostructure for high performance photodetection. *Applied Physics Letters* **120** (2022).